Figure 1: Comparison of SEM micrographs (200x magnification) for three powder batches procured from three separator powder suppliers. All powder batches have a chemical composition consistent with Grade 5 Titanium and nominal size distribution 15-45 microns.

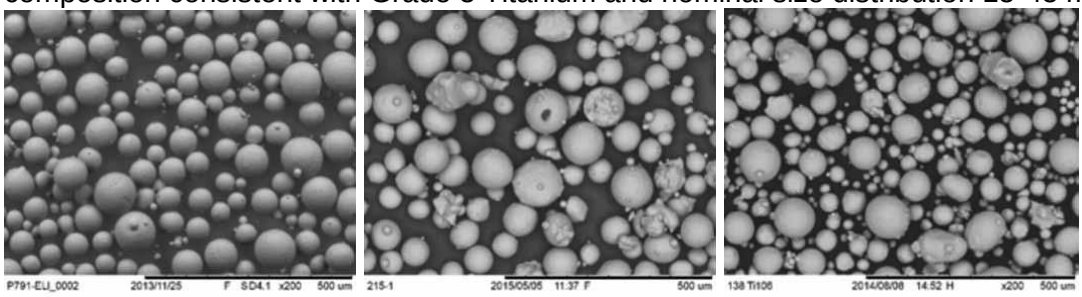

Figure 2: Quantitative particle morphology assessment of powder batches from three suppliers; Black – Supplier (a), Red – Supplier (b), and Blue – Supplier (c).

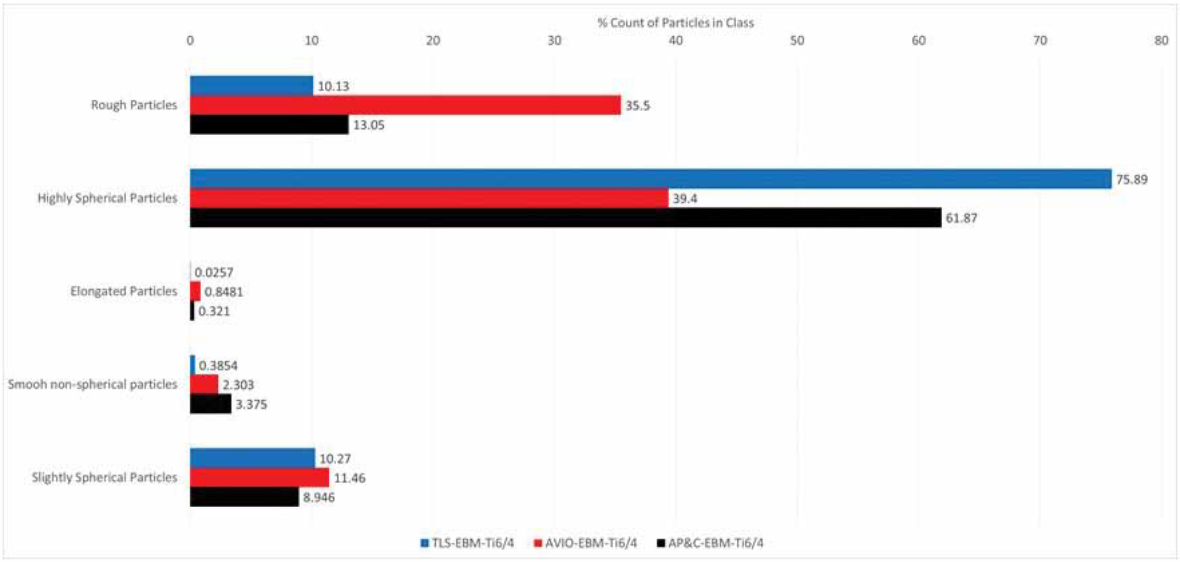

Figure 3: Bulk powder properties (powder flow and packing density) as a function of particle morphology.

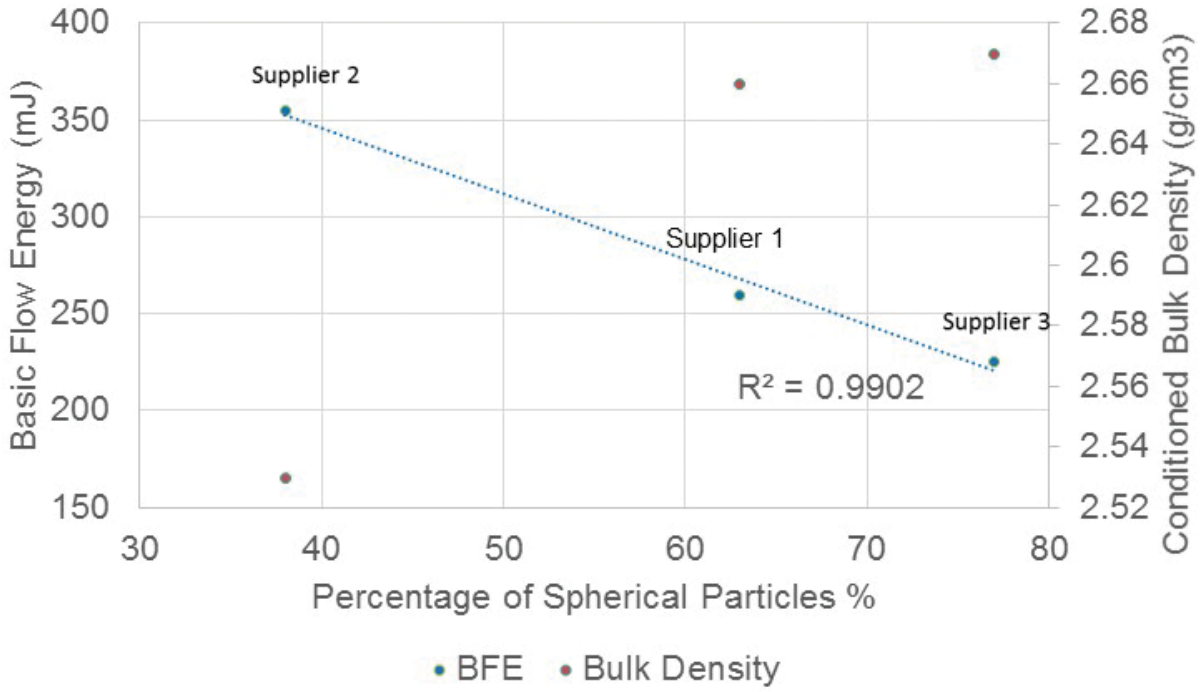

Figure 4 Geometric plot of in-situ shelled canister. Courtesy of the University of Birmingham

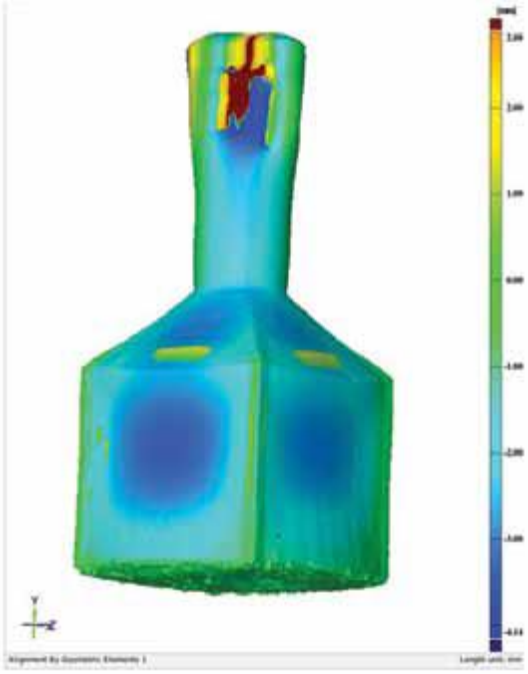

Figure 5 Laser + powder DED. Courtesy of Fraunhofer ILT.

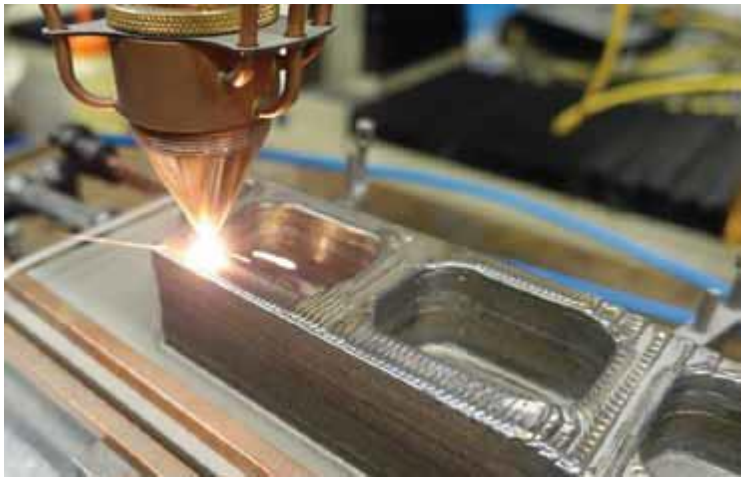

Figure 6 Microstructure of hull and core build strategy in laser melting powder bed fusion. Courtesy of Fraunhofer ILT.

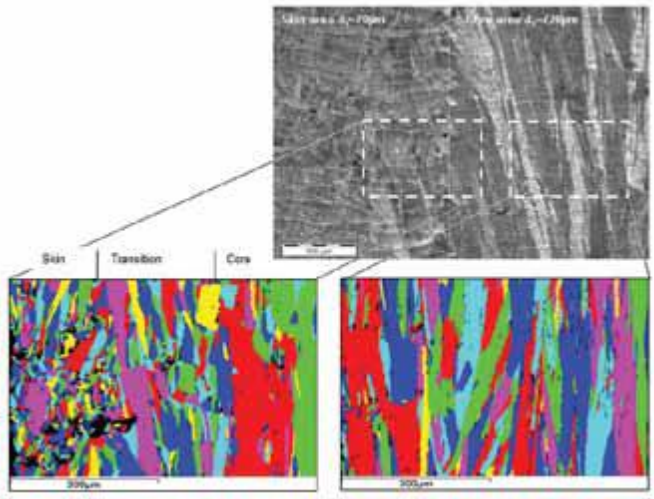

Figure 7 Adaptive Fixture by the MTC, Thales Alenia sun sensor bracket.

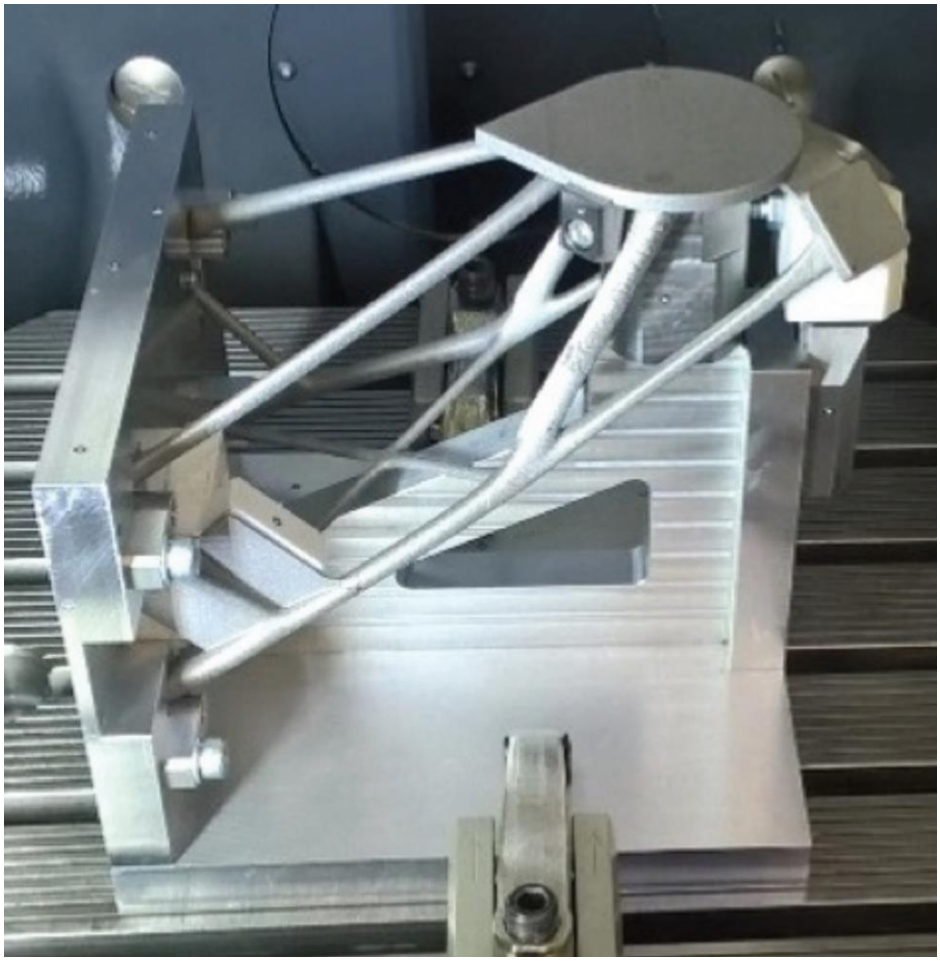

Figure 8 BCT System concept – adaptive machining

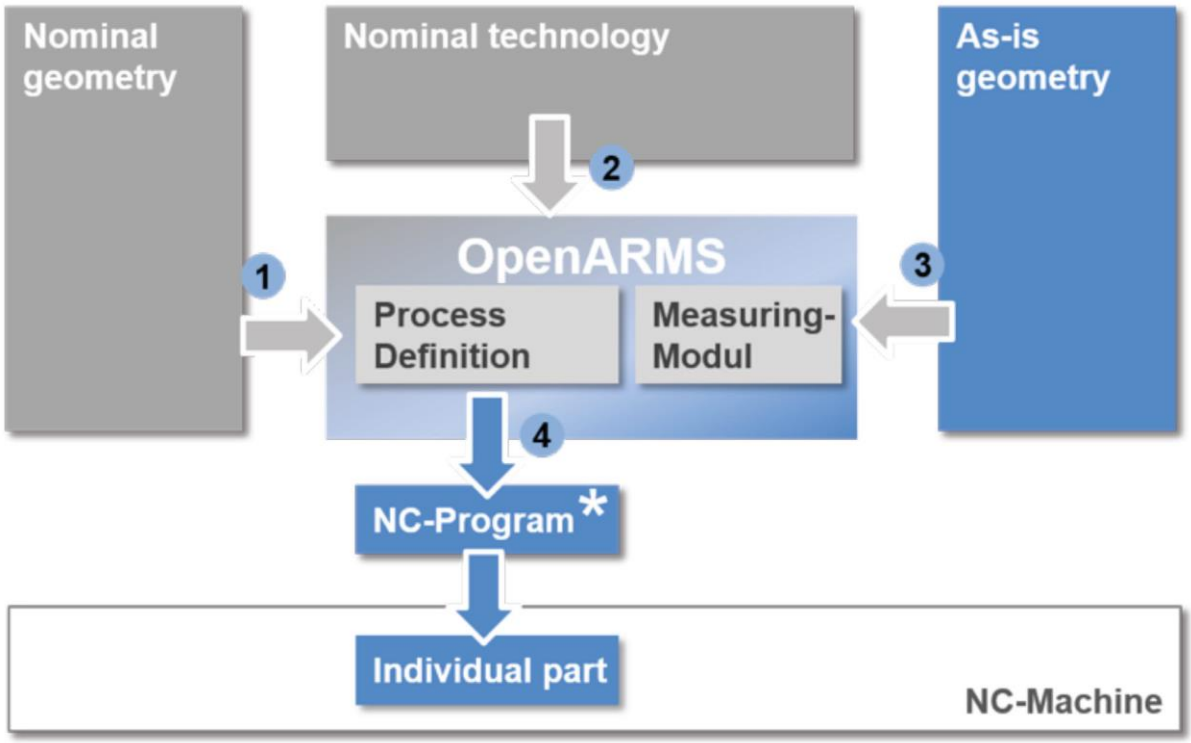

Figure 9 Fraunhofer ILT laser polishing of IN718 compared to Am as built part.

Figure 10 Integration of different in-situ monitoring systems into the WAAM machine head.

Figure 11 Image from blown powder thermal camera.

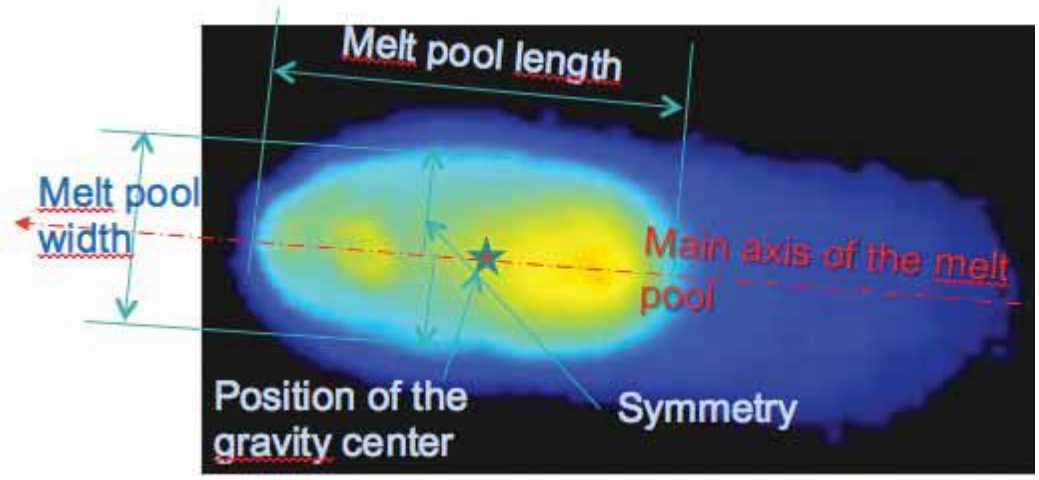

Figure 12 LMD process and measuring head

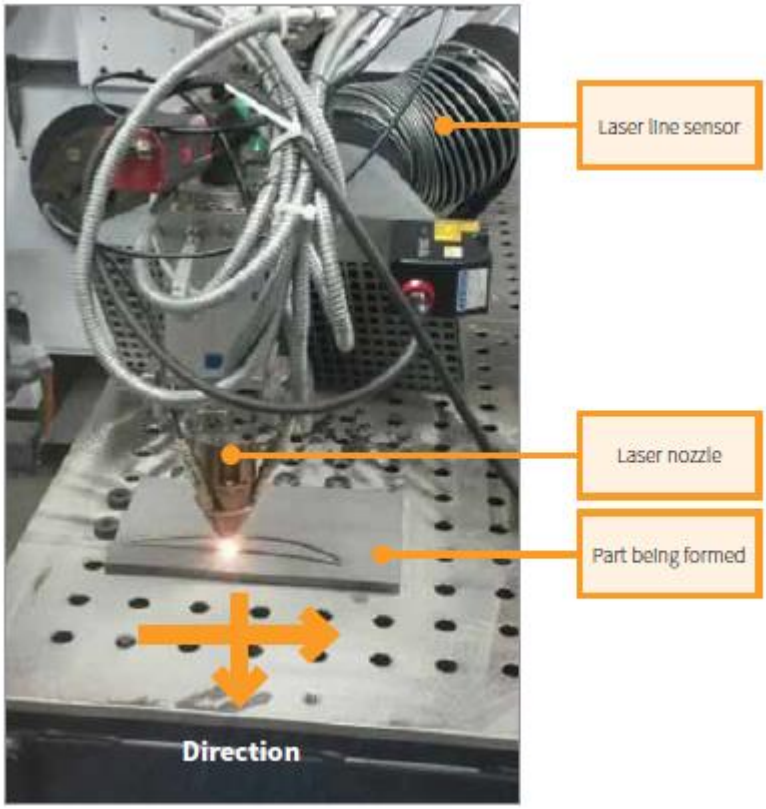

Figure 13 Integration of thermal camera in the IREPA blown powder system

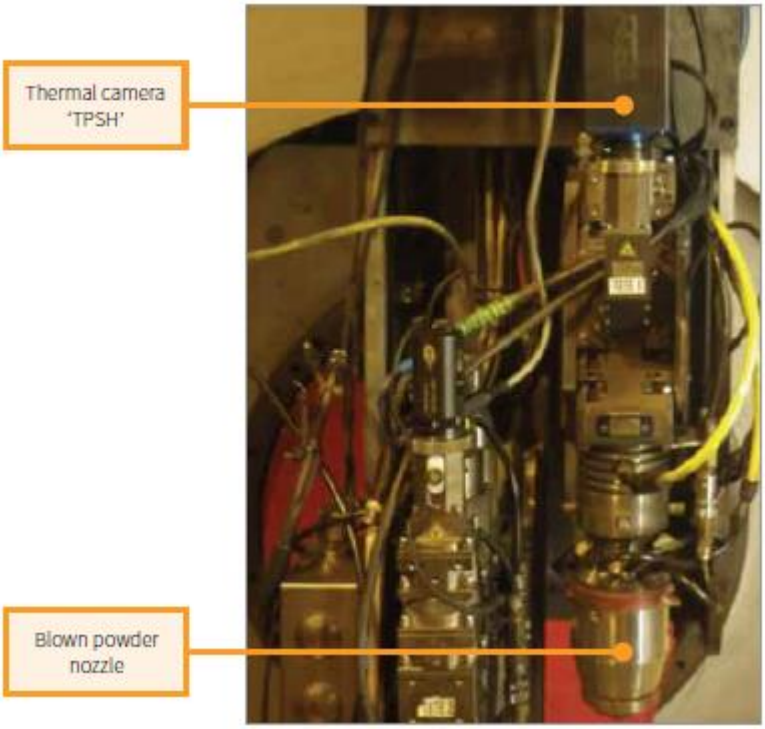

Figure 14 Powder bed supply interacting with coaxial laser in powder bed processes.

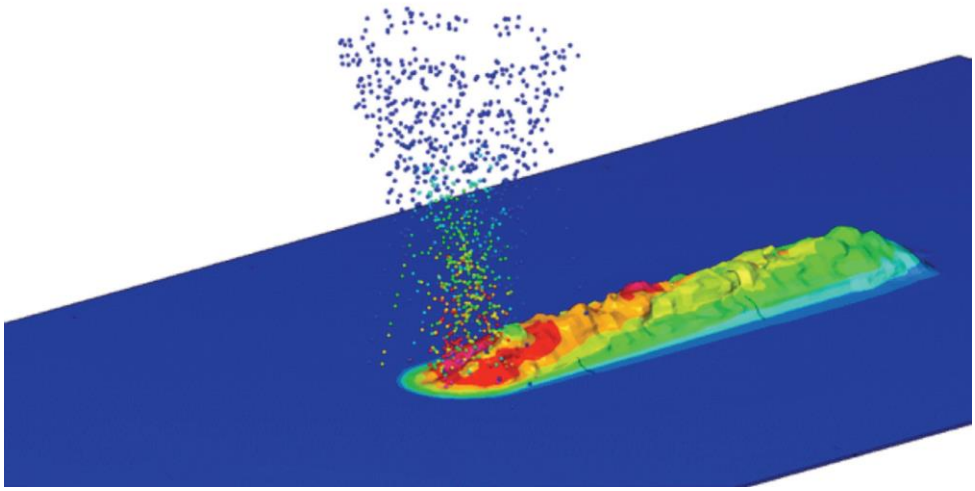

Figure 15 Surface roughness of molybdenum processed via powder bed fusion.

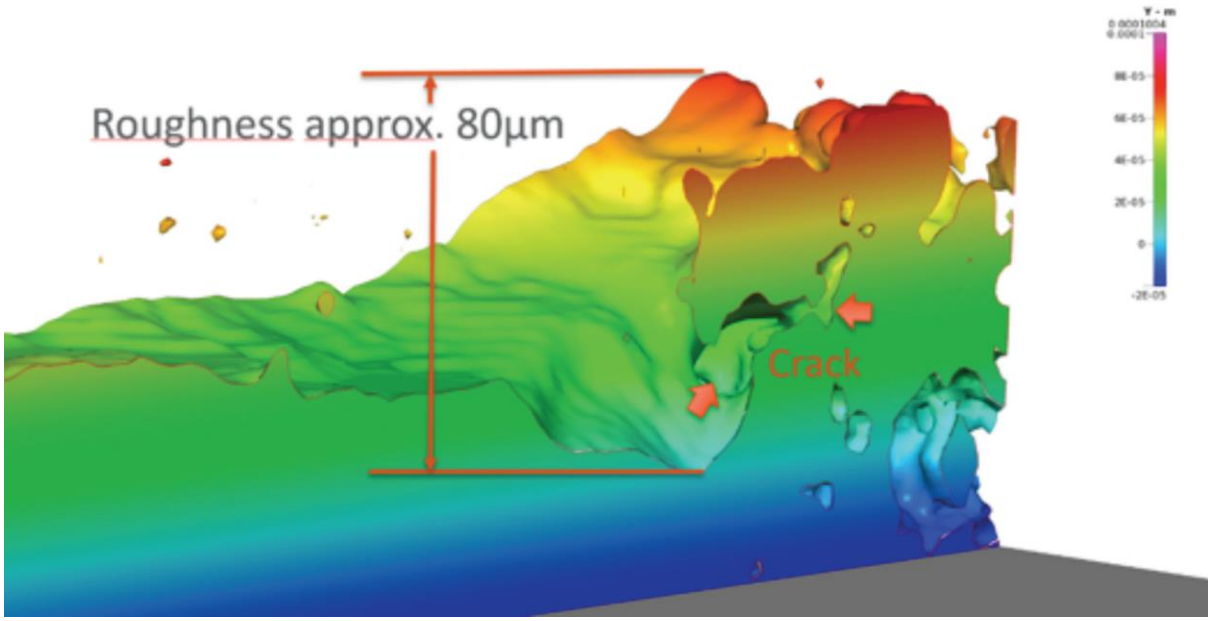

Figure 16 Component scale models resolve the large-scale processes providing insight on manufacturability and whether the final product will be conformal to the original design.

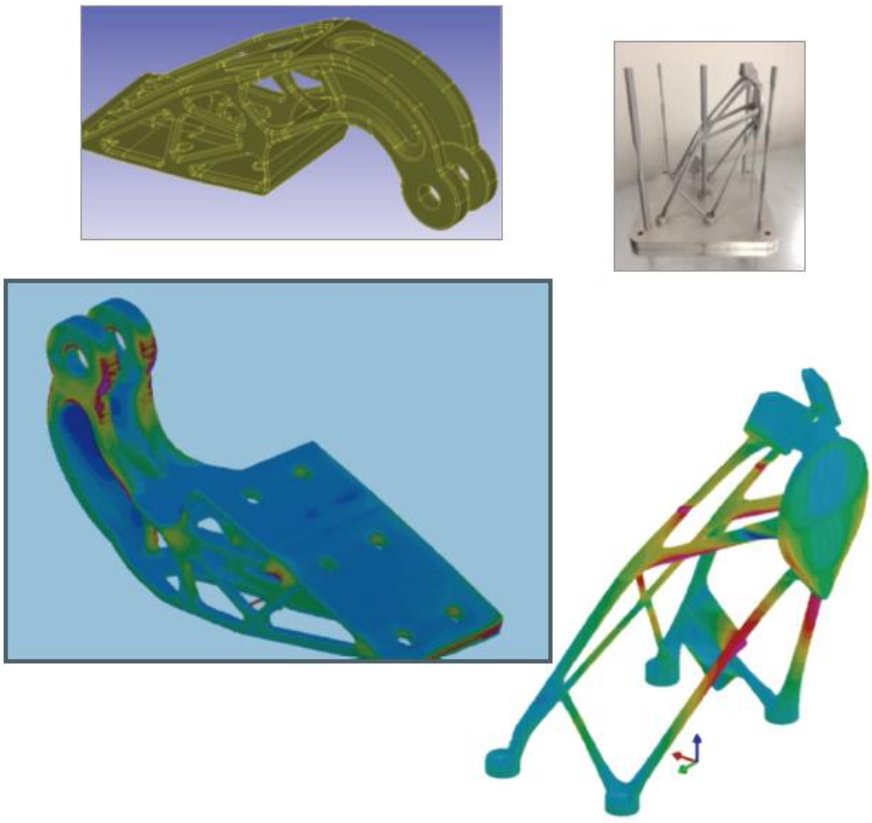

Figure 17 Four AM factory locations.

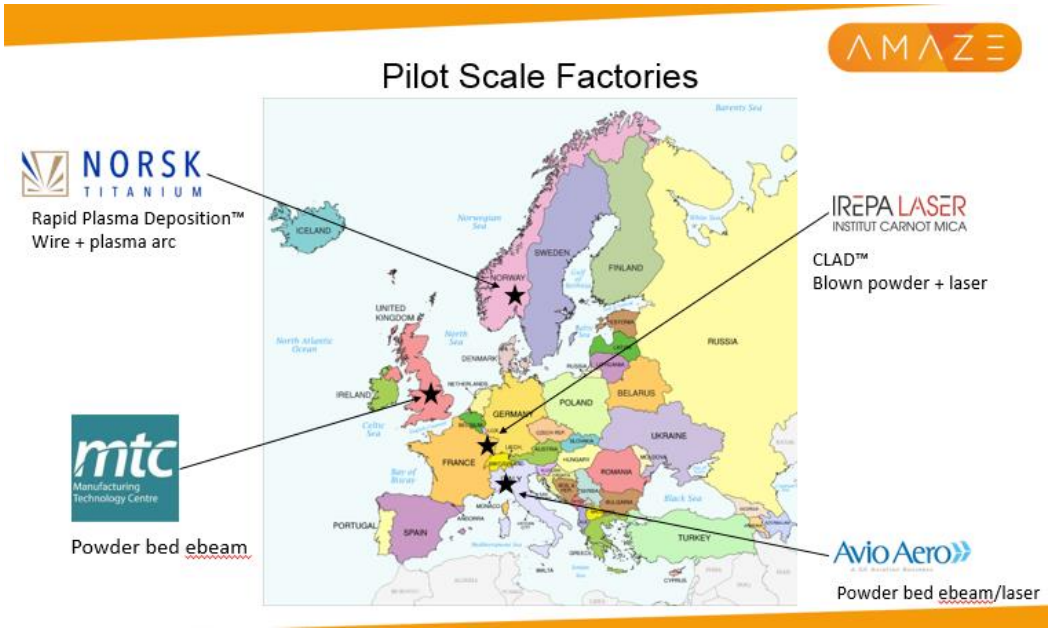

Figure 18 Norsk Titanium AM Machine Rapid plasma deposition

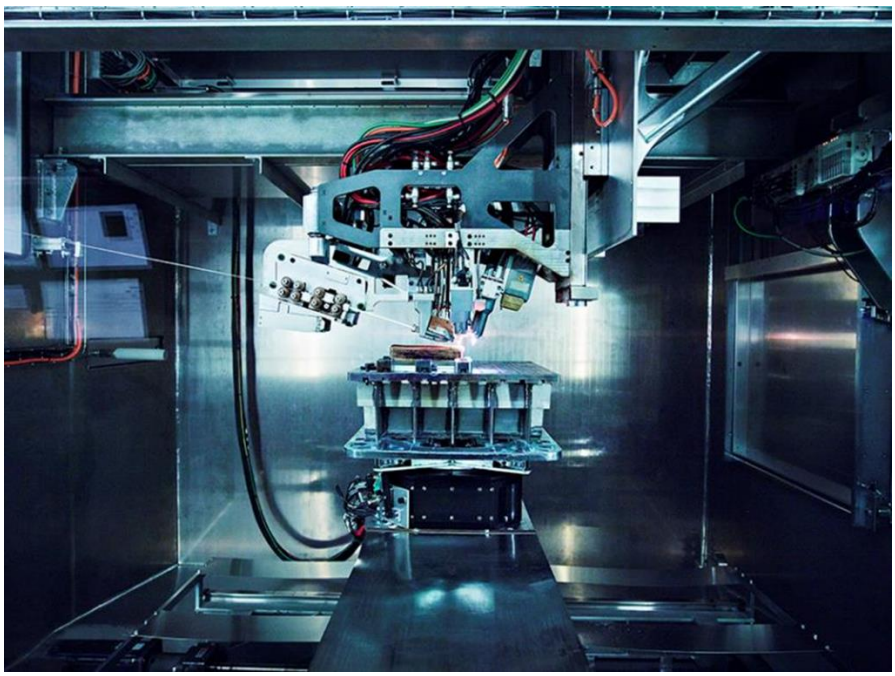

Figure 19 AMAZE APOD 12 ESA Cylinder Laser Blow Powder by Irepa Laser

Figure 20 Plan for Thales – Sun sensor APOD

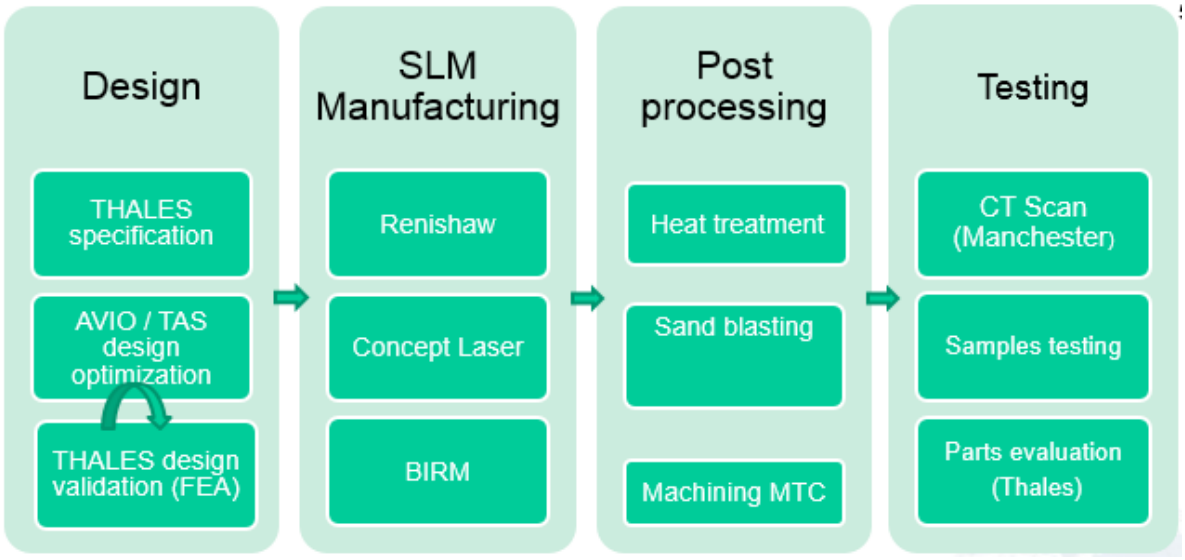

Figure 21 Final Design achievement for sun sensor – Thales Alenia space.

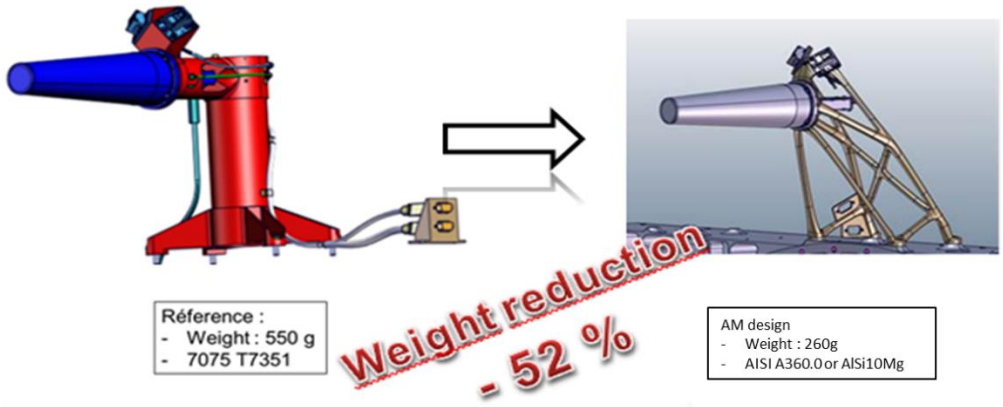

Figure 22 Non-destructive testing by neutron diffraction (ILL)

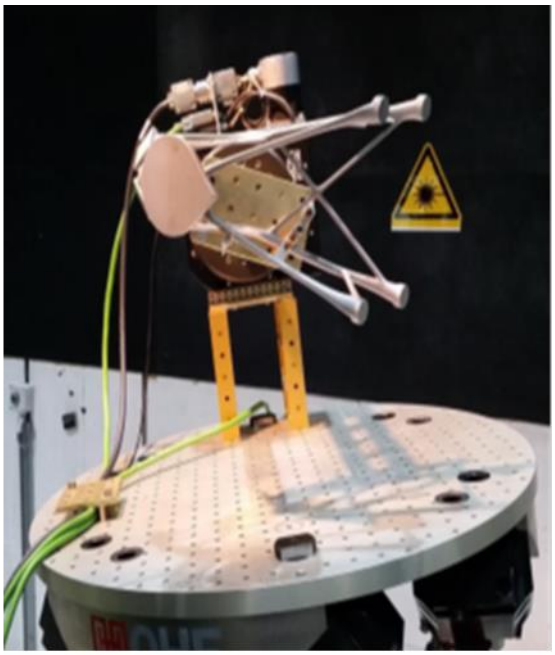

Figure 23 Tungsten deposit

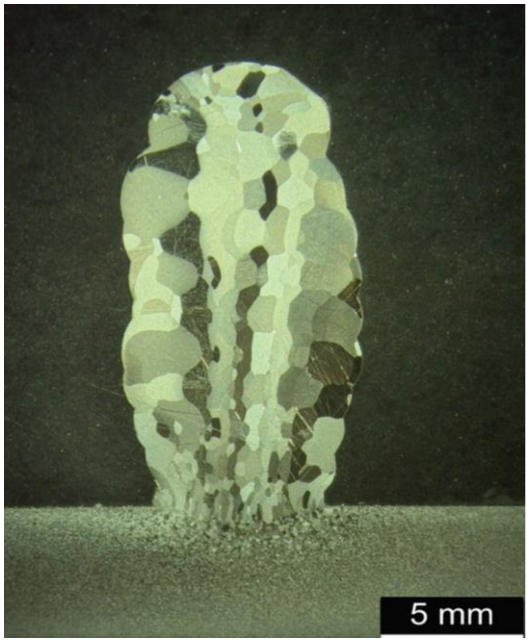

Figure 24 In-process cold-worked titanium

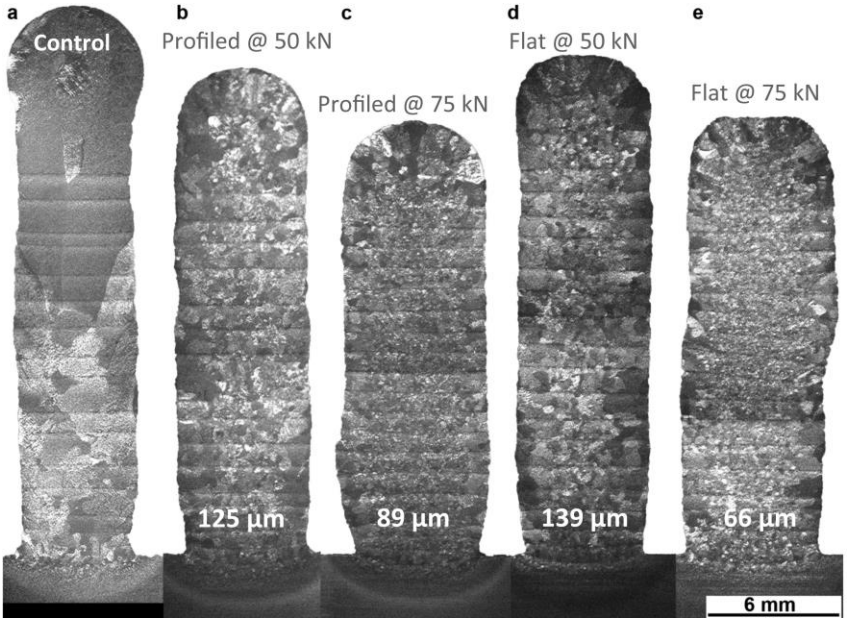

Figure 25 Nanoindentation maps of AlSi10Mg and Al-Si-Ni cross-sections.

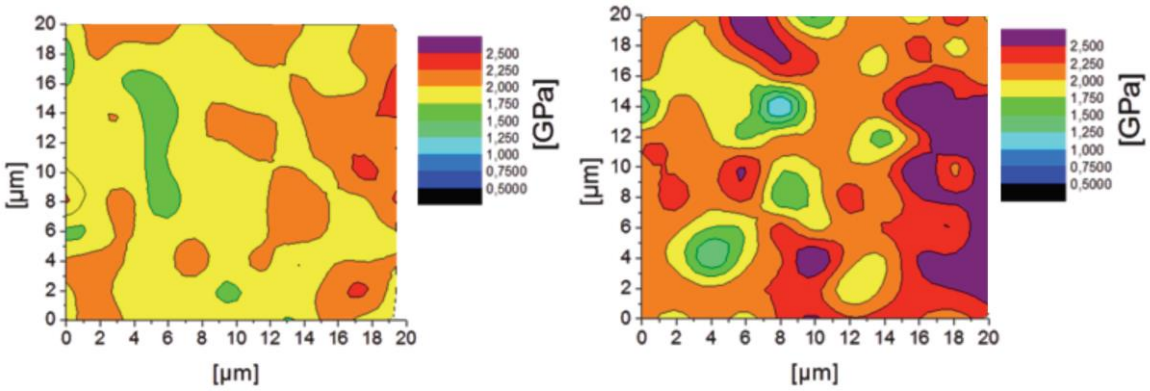

Figure 26 Stress strain curves of A357 samples built with different building platform temperatures.

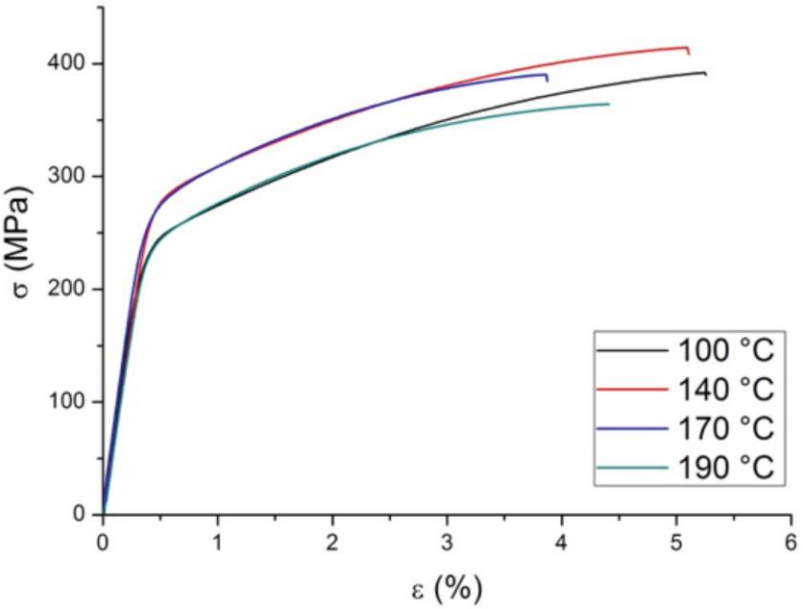

Figure 27 Process window of the AlSi10Mg powder, chosen based on optical microscopy on-top images

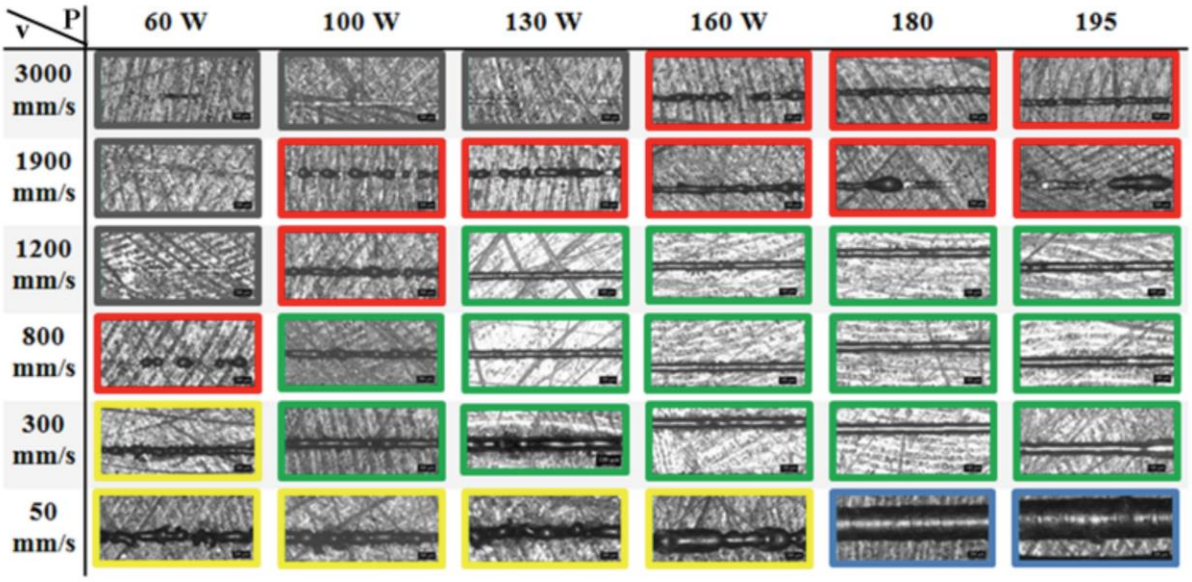

Figure 28 Wöhler diagram for TiAl6V4 produced by different methods of additive manufacturing compared to the data for conventionally processed samples.

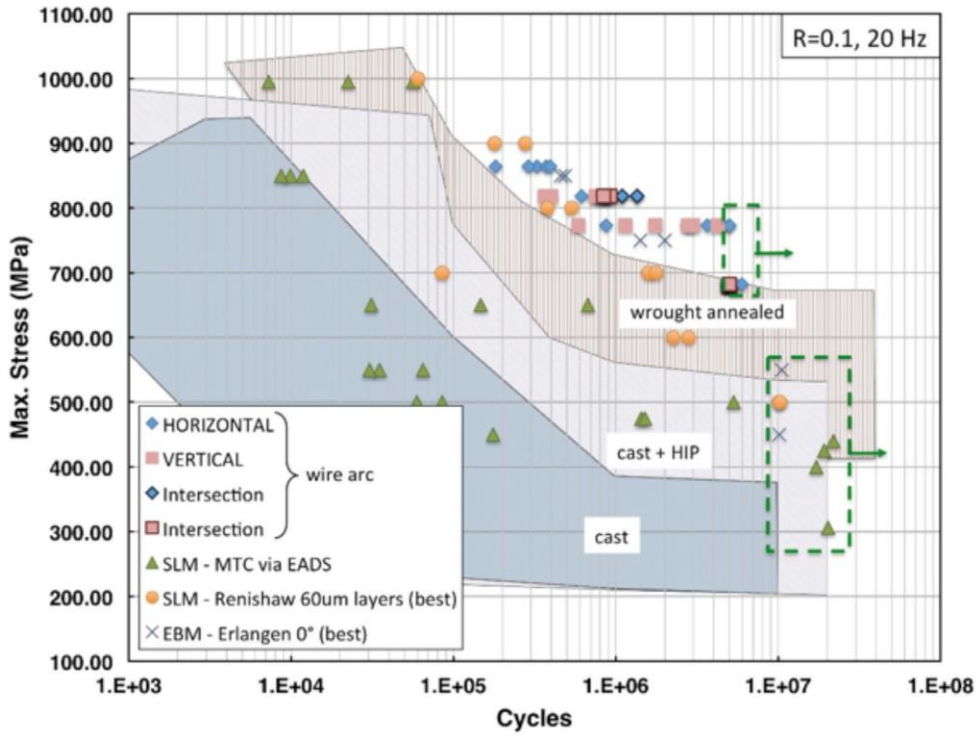

Figure 29 Strain distribution map in a TiAl6V4 sample made by wire arc deposition after various strains. The region of localisation can already be guessed in the picture at 3.5% strain, i.e. before the stress maximum.

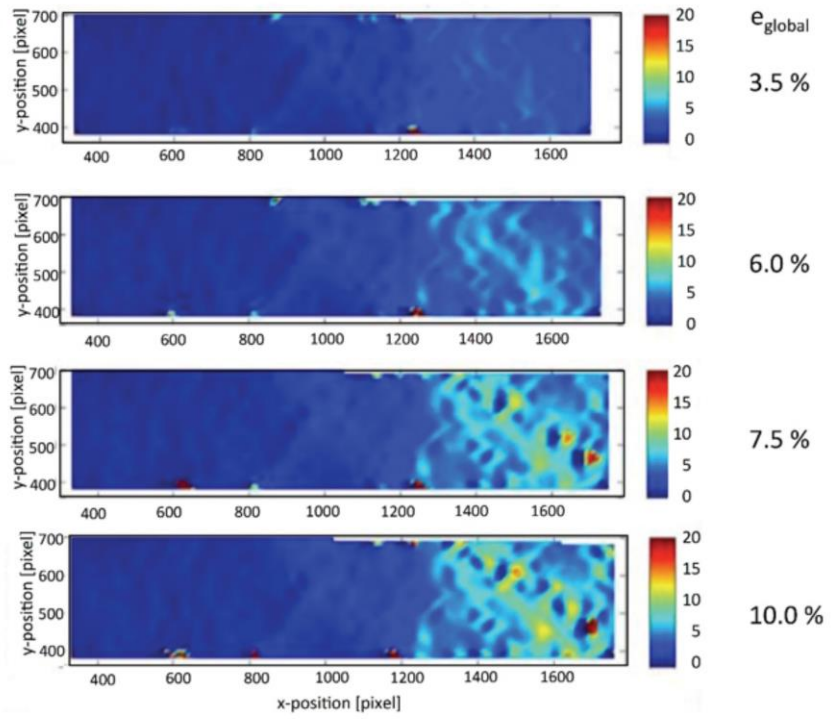

Figure 30 Invar36 components produced for Airbus

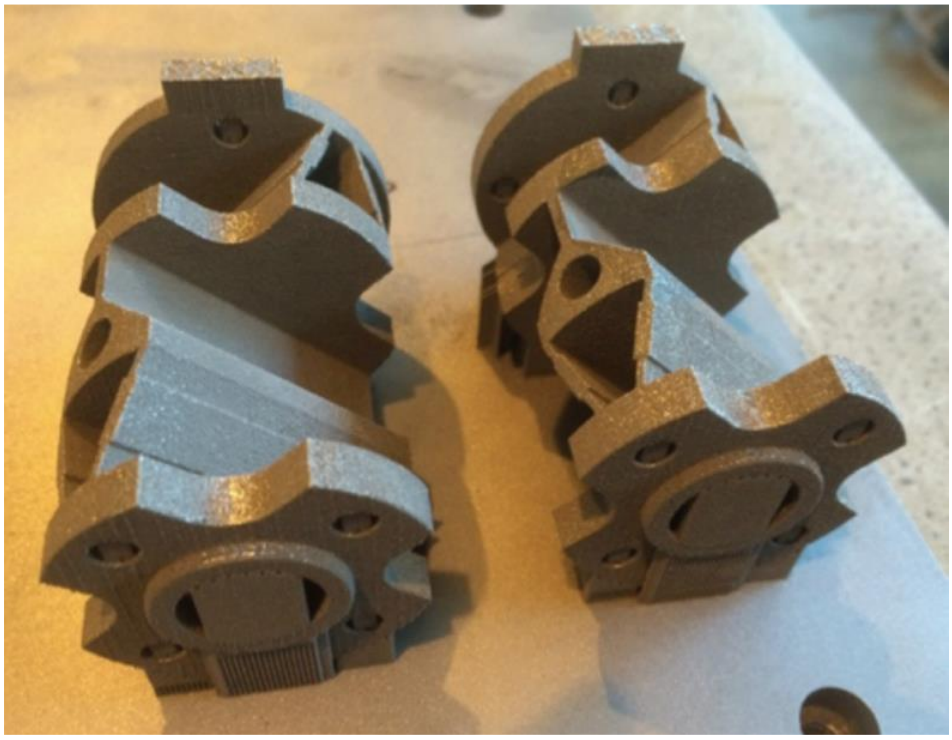

Figure 31 Alloying aluminium and silicon elemental powders by selective laser melting.

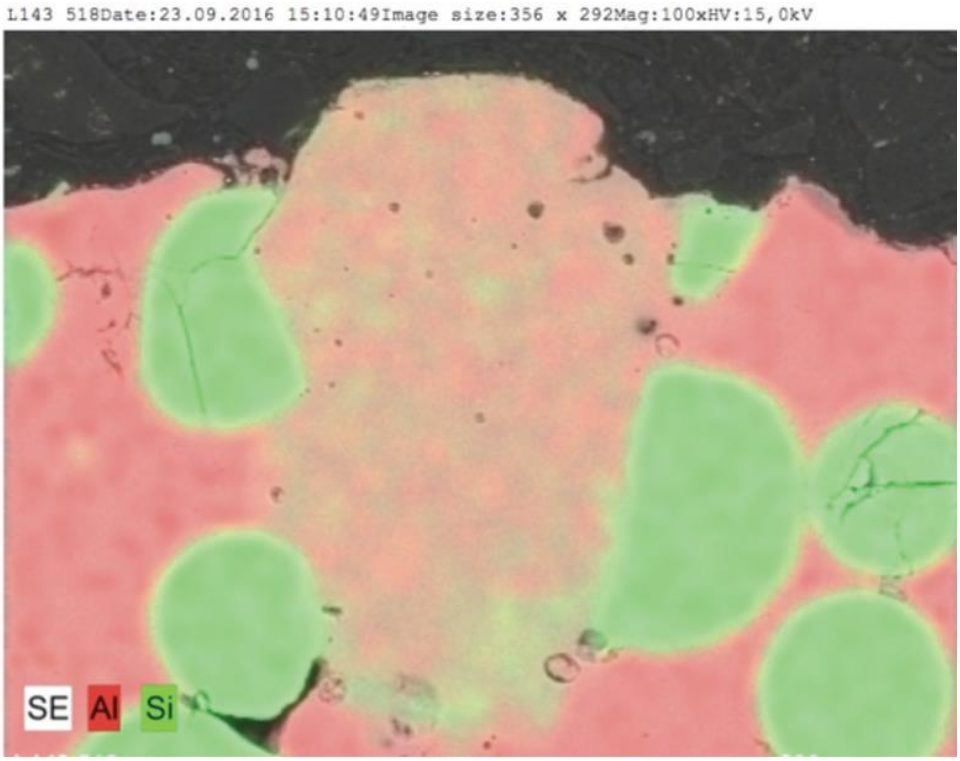

Figure 32 Process optimisation for the production of fully dense AlSix by selective laser melting.

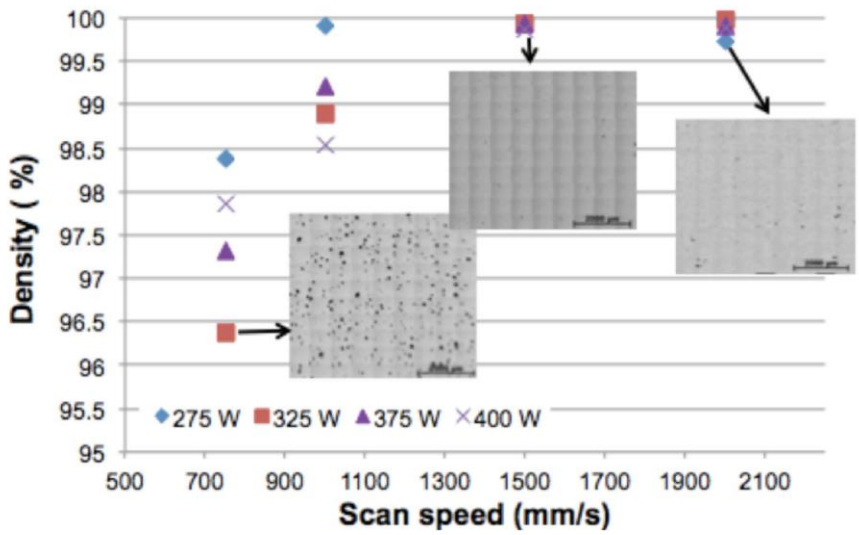

Figure 33 3D quadratic chiral auxetic structures (Ti-6Al-V4, node distance: 5 mm).

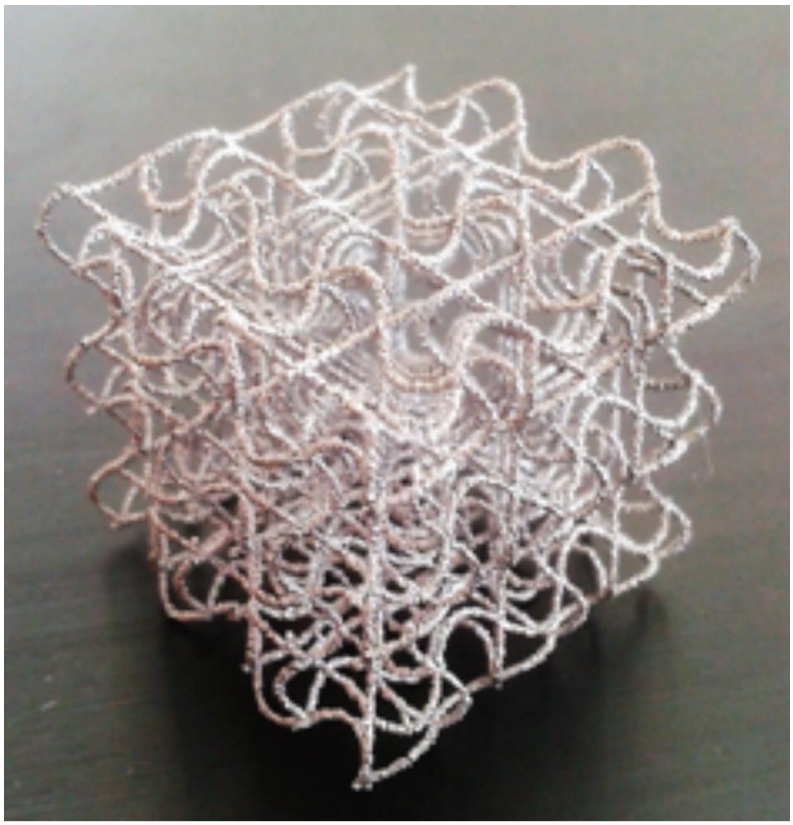

Figure 34

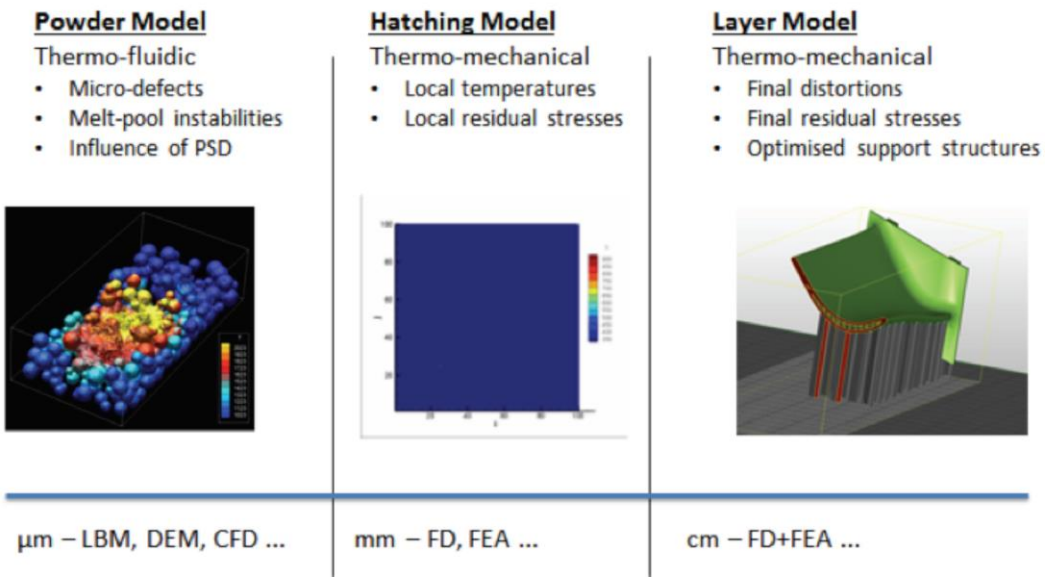

Figure 35 Test plate produced from SLM fabricated Mo powder.

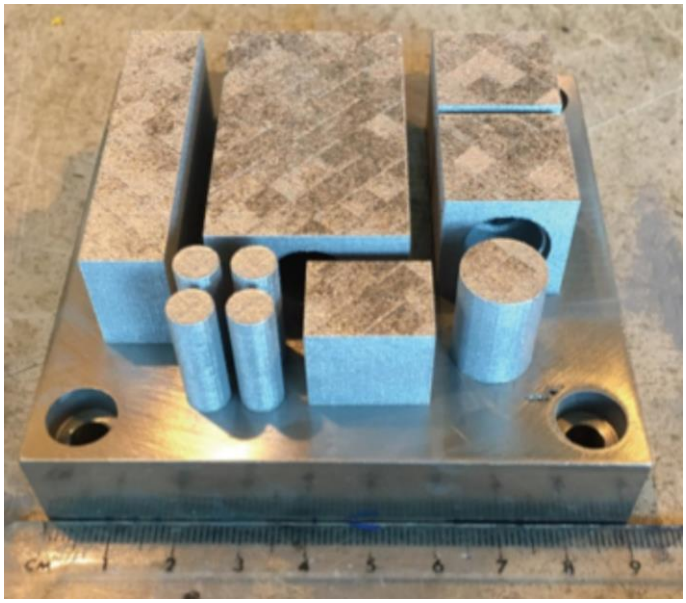

Figure 36 SEM micrograph showing defect formation in SLM fabricated Mo.

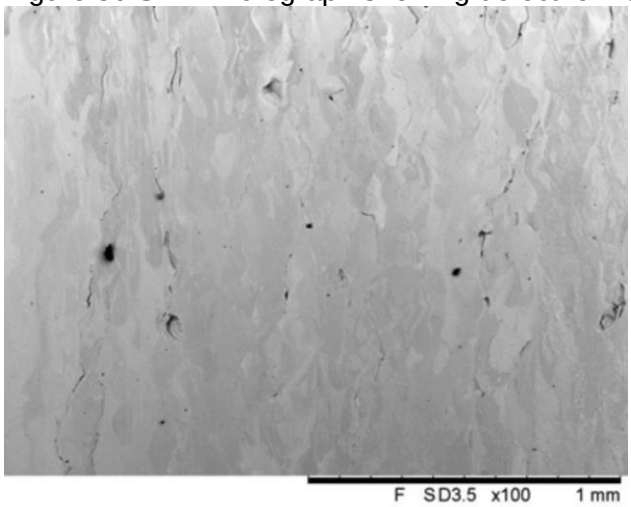

Figure 37 Micrograph showing HIP diffusion bond between Mo and W.